






Article

# Electrostatic Self-Assembly of CdS Quantum Dots with Co<sub>9</sub>S<sub>8</sub> Hollow Nanotubes for Enhanced Visible Light Photocatalytic H<sub>2</sub> Production

Yuqing Yan <sup>1</sup>, Yonghui Wu <sup>1</sup>, Chenggen Lu <sup>1</sup>, Yu Wei <sup>1</sup>, Jun Wang <sup>1</sup>, Bo Weng <sup>2</sup> , Wei-Ya Huang <sup>1</sup> , Jia-Lin Zhang <sup>1</sup> , Kai Yang <sup>1</sup>  and Kangqiang Lu <sup>1,\*</sup> 

- <sup>1</sup> Jiangxi Provincial Key Laboratory of Functional Crystalline Materials Chemistry, School of Chemistry and Chemical Engineering, Jiangxi University of Science and Technology, Ganzhou 341000, China; 18797912889@163.com (Y.Y.); 13207070350@163.com (Y.W.); 17779524039@163.com (C.L.); 18225906201@163.com (Y.W.); wj15270473375@126.com (J.W.); hweiya@126.com (W.-Y.H.); jialinz2007@163.com (J.-L.Z.); yangkai@jxust.edu.cn (K.Y.)
- <sup>2</sup> CAS Key Laboratory of Urban Pollutant Conversion, Institute of Urban Environment, Chinese Academy of Sciences, Xiamen 361021, China; bweng@iue.ac.cn
- \* Correspondence: kqlu@jxust.edu.cn

**Abstract:** CdS quantum dots (CdS QDs) are regarded as a promising photocatalyst due to their remarkable response to visible light and suitable placement of conduction bands and valence bands. However, the problem of photocorrosion severely restricts their application. Herein, the CdS QDs-Co<sub>9</sub>S<sub>8</sub> hollow nanotube composite photocatalyst has been successfully prepared by loading Co<sub>9</sub>S<sub>8</sub> nanotubes onto CdS QDs through an electrostatic self-assembly method. The experimental results show that the introduction of Co<sub>9</sub>S<sub>8</sub> cocatalyst can form a stable structure with CdS QDs, and can effectively avoid the photocorrosion of CdS QDs. Compared with blank CdS QDs, the CdS QDs-Co<sub>9</sub>S<sub>8</sub> composite exhibits obviously better photocatalytic hydrogen evolution performance. In particular, CdS QDs loaded with 30% Co<sub>9</sub>S<sub>8</sub> (CdS QDs-30%Co<sub>9</sub>S<sub>8</sub>) demonstrate the best photocatalytic performance, and the H<sub>2</sub> production rate reaches 9642.7 μmol·g<sup>-1</sup>·h<sup>-1</sup>, which is 60.3 times that of the blank CdS QDs. A series of characterizations confirm that the growth of CdS QDs on Co<sub>9</sub>S<sub>8</sub> nanotubes effectively facilitates the separation and migration of photogenerated carriers, thereby improving the photocatalytic hydrogen production properties of the composite. We expect that this work will facilitate the rational design of CdS-based photocatalysts, thereby enabling the development of more low-cost, high-efficiency and high-stability composites for photocatalysis.

**Keywords:** CdS; Co<sub>9</sub>S<sub>8</sub>; quantum dot; photocatalytic H<sub>2</sub> evolution; cocatalyst



**Citation:** Yan, Y.; Wu, Y.; Lu, C.; Wei, Y.; Wang, J.; Weng, B.; Huang, W.-Y.; Zhang, J.-L.; Yang, K.; Lu, K. Electrostatic Self-Assembly of CdS Quantum Dots with Co<sub>9</sub>S<sub>8</sub> Hollow Nanotubes for Enhanced Visible Light Photocatalytic H<sub>2</sub> Production. *Molecules* **2024**, *29*, 3530. <https://doi.org/10.3390/molecules29153530>

Academic Editor: Eun Duck Park

Received: 21 June 2024  
Revised: 25 July 2024  
Accepted: 25 July 2024  
Published: 26 July 2024



**Copyright:** © 2024 by the authors. Licensee MDPI, Basel, Switzerland. This article is an open access article distributed under the terms and conditions of the Creative Commons Attribution (CC BY) license (<https://creativecommons.org/licenses/by/4.0/>).

## 1. Introduction

With the increasingly serious environmental pollution and the increasing demand for energy, the development and utilization of sustainable clean energy to achieve green development has become a hot topic [1–4]. In recent years, photocatalytic hydrogen evolution has attracted much attention due to its advantages of zero carbon emission, high efficiency and sustainability, and is considered a promising energy conversion method [5–7]. Therefore, the utilization of photocatalytic technology to produce hydrogen energy represents a feasible strategy for alleviating environmental pollution and energy crises [8–10]. The practical application of photocatalytic hydrogen production technology is contingent upon three key factors: low cost, high efficiency and high stability [11,12]. One of the most commonly employed modification strategies to improve the photocatalytic H<sub>2</sub> evolution properties of semiconductors is the introduction of precious metals (such as Au, Ag, Pd and Pt) through doping. Nevertheless, precious metals are limited and expensive. Consequently, the development of cost-effective, environmentally friendly and highly active photocatalysts represents a significant and pressing challenge [13,14].

In recent years, metal sulfides have become a research focus in the field of photocatalytic hydrogen evolution on account of their exceptional light absorption properties and unique electronic structure. Among these, CdS has been extensively studied owing to its appropriate band gap and position of energy bands [15,16]. Moreover, CdS exhibits diverse morphologies and structures, involving zero-dimensional (0D) quantum dots, one-dimensional (1D) nanorods, two-dimensional (2D) nanosheets and three-dimensional (3D) cubes [17]. CdS QDs are considered to be a promising photocatalytic material due to their small size (<10 nm), high electron mobility and abundant recoverable light [18,19]. However, the issue of easy hole oxidation decomposition (photocorrosion) severely restricts the application of CdS [20]. Among various strategies to alleviate CdS photocorrosion, the rational incorporation of a cocatalyst is an effective approach [21]. Co<sub>9</sub>S<sub>8</sub> serves as a widely used cocatalyst with advantages such as easy availability, abundant active sites and adjustable chemical composition [22]. In particular, the hollow-structured Co<sub>9</sub>S<sub>8</sub> possesses a large specific surface area and enhances the absorption of light by multiple reflections, which is of significant importance in improving photocatalytic properties. Additionally, the electrostatic self-assembly method is an efficient and environmentally friendly preparation method for nanoparticles, which is expected to prepare highly active photocatalysts [23].

Herein, the CdS QDs-Co<sub>9</sub>S<sub>8</sub> composite photocatalyst is successfully prepared through electrostatic self-assembly. Compared to blank CdS QDs, the CdS QDs-Co<sub>9</sub>S<sub>8</sub> composite demonstrates enhanced photocatalytic H<sub>2</sub> production performance. Notably, the optimal CdS QDs-30%Co<sub>9</sub>S<sub>8</sub> exhibits a photocatalytic hydrogen production rate of 9642.7 μmol·g<sup>-1</sup>·h<sup>-1</sup>, approximately 60.3 times that of blank CdS QDs. Cyclic experiments indicate that the introduction of Co<sub>9</sub>S<sub>8</sub> cocatalyst effectively prevents photocorrosion on the surface of CdS QDs. Moreover, subsequent characterizations confirm that loading Co<sub>9</sub>S<sub>8</sub> cocatalyst effectively promotes the separation and migration of photogenerated carriers, thereby improving the photocatalytic properties of CdS QDs. This work illustrates the significant role of Co<sub>9</sub>S<sub>8</sub> as a cocatalyst in the field of photocatalytic H<sub>2</sub> production, and is expected to provide a useful reference for the development of effective and stable photocatalysts.

## 2. Results and Discussion

The synthesis process of the CdS QDs-Co<sub>9</sub>S<sub>8</sub> composite photocatalyst is shown in Figure 1. Initially, the Co<sub>9</sub>S<sub>8</sub> nanotubes are achieved through a two-step hydrothermal approach, followed by treatment with APTES to impart a positive charge. Subsequently, the treated Co<sub>9</sub>S<sub>8</sub> nanotubes are subjected to an electrostatic assembly process with CdS QDs, resulting in the formation of the CdS QDs-Co<sub>9</sub>S<sub>8</sub> composite photocatalyst. A diagram of the prepared samples diagram is depicted in Figure S1. As illustrated in Figure S1a,b, CdS QDs exhibit a yellow powder, while Co<sub>9</sub>S<sub>8</sub> nanotubes display a black powder. Upon assembly of CdS QDs and Co<sub>9</sub>S<sub>8</sub> nanotubes, the resulting CdS QDs-Co<sub>9</sub>S<sub>8</sub> composite appears yellowish-green (Figure S1c).

Figure 2a,b display the Zeta potentials of APTES-modified Co<sub>9</sub>S<sub>8</sub> and CdS QDs suspension dispersed in deionized water, respectively. It can be observed that the Zeta potentials of APTES-modified Co<sub>9</sub>S<sub>8</sub> and CdS QDs are 13.8 mV and −30 mV, respectively, which means that APTES-modified Co<sub>9</sub>S<sub>8</sub> is positively charged, while CdS QDs is negatively charged. This result provides a good basis for the assembly of the CdS QDs-Co<sub>9</sub>S<sub>8</sub> composite [24].

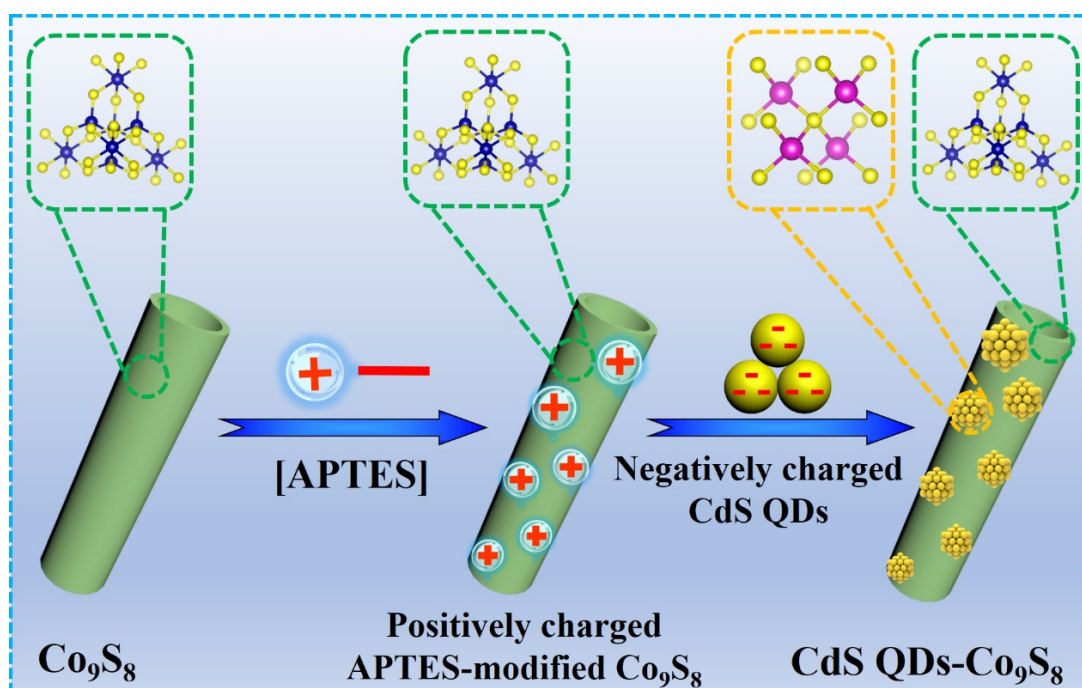


Figure 1. Synthesis diagram of CdS QDs-Co<sub>9</sub>S<sub>8</sub> composite photocatalyst.

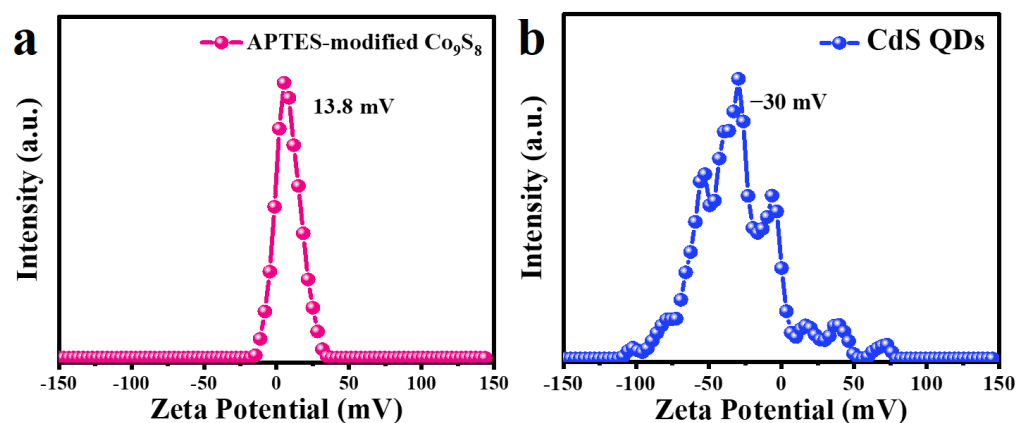
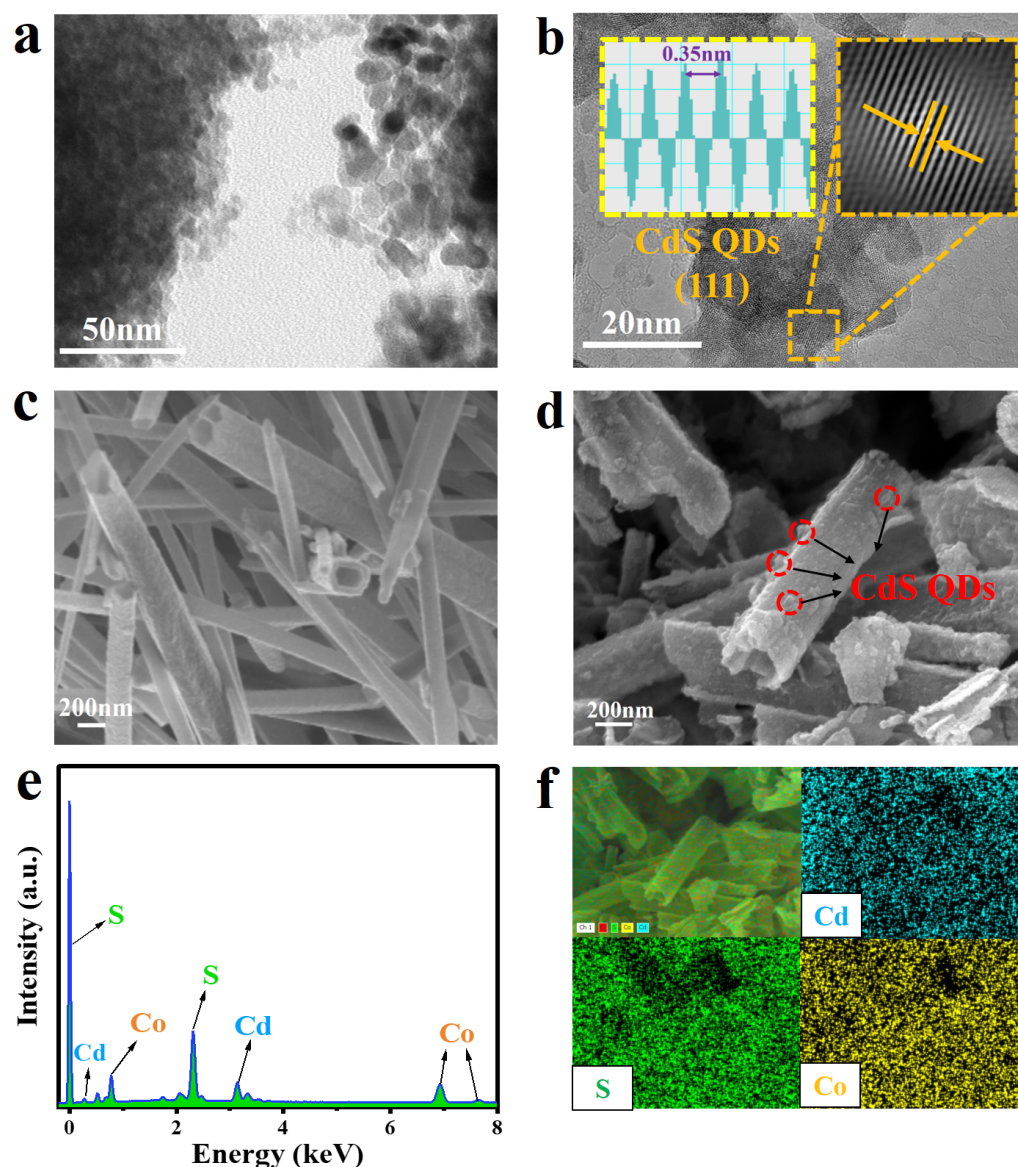


Figure 2. Zeta potential of (a) APTES-modified Co<sub>9</sub>S<sub>8</sub> and (b) CdS QDs suspension dispersed in deionized water.

Morphological and microstructural analyses of CdS QDs, Co<sub>9</sub>S<sub>8</sub> and CdS QDs-30%Co<sub>9</sub>S<sub>8</sub> were conducted using scanning electron microscopy (SEM) and transmission electron microscope (TEM). As shown in Figure 3a, the TEM image reveals that the diameter of CdS QDs is roughly 4 nm, consistent with previous literature [25]. Furthermore, as displayed in Figure 3b, the high-resolution TEM (HRTEM) image exhibits a lattice spacing of 0.35 nm corresponding to the (111) crystal face of CdS QDs, indicating its successful preparation [25]. Meanwhile, the TEM and HRTEM images of Co<sub>9</sub>S<sub>8</sub> (Figure S2) demonstrate the successful synthesis of Co<sub>9</sub>S<sub>8</sub> nanotubes. As depicted in Figure S2b, the 0.23 nm of lattice spacing corresponds to the (420) crystal face of Co<sub>9</sub>S<sub>8</sub>. Figure 3c illustrates a hollow nanotube structure with a diameter of approximately 200 nm for Co<sub>9</sub>S<sub>8</sub>. As exhibited in Figure 3d, CdS QDs-30%Co<sub>9</sub>S<sub>8</sub> inherits the hollow nanotube structure of Co<sub>9</sub>S<sub>8</sub>. It is worth noting that the hollow structure exposes a large specific surface area and enhances the absorption of light by multiple reflections, which is of significant importance in improving the photocatalytic properties. Furthermore, it can be observed that CdS QDs are evenly decentralized on the Co<sub>9</sub>S<sub>8</sub> nanotubes. As presented in Figure 3e, the EDS spectra illustrate the presence of Co, Cd and S elements in the CdS QDs-30%Co<sub>9</sub>S<sub>8</sub> composite. Moreover, the composition

of all the composite photocatalysts is quantitatively analyzed using inductively coupled plasma emission spectrometry (ICP-OES). As indicated in Table S1, as the  $\text{Co}_9\text{S}_8$  load increases, the proportion of the Co element rises, while the proportion of the Cd element decreases, consistent with the anticipated results. In addition, the element mapping results of CdS QDs-30% $\text{Co}_9\text{S}_8$  indicate that CdS QDs are uniformly distributed on the surface of  $\text{Co}_9\text{S}_8$  nanotubes (Figure 3f). These results demonstrate the successful synthesis of the CdS QDs-30% $\text{Co}_9\text{S}_8$  composite.



**Figure 3.** (a) TEM image and (b) HRTEM image of CdS QDs. SEM images of (c)  $\text{Co}_9\text{S}_8$  and (d) CdS QDs-30% $\text{Co}_9\text{S}_8$ . (e) The EDS spectrum of CdS QDs-30% $\text{Co}_9\text{S}_8$ . (f) The element mapping results of CdS QDs-30% $\text{Co}_9\text{S}_8$ .

The crystal structure and phase composition of the prepared samples were investigated by X-ray diffraction (XRD). Figure 4a illustrates the XRD patterns of CdS QDs,  $\text{Co}_9\text{S}_8$  and CdS QDs-30% $\text{Co}_9\text{S}_8$ . It can be observed that the XRD peak of CdS exhibits a relatively strong intensity, indicating its robust crystal phase. In contrast, the XRD peak of  $\text{Co}_9\text{S}_8$  displays a relatively weak intensity, suggesting its inferior crystal phase. For  $\text{Co}_9\text{S}_8$ , the diffraction peaks at  $2\theta = 29.9^\circ, 31.4^\circ, 37.4^\circ, 39.5^\circ, 47.5^\circ, 52.3^\circ$  and  $54.6^\circ$  correspond to the crystal planes (311), (222), (400), (331), (511), (400) and (531) of  $\text{Co}_9\text{S}_8$ , respectively (JCPDS: 65-1765) [26]. As for CdS QDs, the characteristic peaks at  $26.2^\circ, 43.6^\circ$  and  $51.7^\circ$  can be

related to the crystal faces (111), (220) and (311) of CdS (JCPDS: 75-1546), respectively [27]. In addition, the XRD diffraction curve of CdS QDs-30%Co<sub>9</sub>S<sub>8</sub> is highly similar to that of CdS QDs, except that a weak peak at 39.5° belongs to the (331) crystal plane of Co<sub>9</sub>S<sub>8</sub>, demonstrating the successful assembly of the CdS QDs-Co<sub>9</sub>S<sub>8</sub> composite. Furthermore, the (111) crystal face of CdS QDs exhibits a strong characteristic diffraction peak, resulting in a peak of Co<sub>9</sub>S<sub>8</sub> at 29.9° masked by CdS QDs. The optical properties of a series of samples are determined by UV-vis diffuse reflectance spectroscopy (DRS). Figure 4b exhibits the light absorption curves of CdS QDs, Co<sub>9</sub>S<sub>8</sub> and the CdS QDs-30%Co<sub>9</sub>S<sub>8</sub> composite. The blank CdS presents a distinct absorption edge at near 570 nm. Moreover, Co<sub>9</sub>S<sub>8</sub> illustrates strong absorption across the entire spectral range, suggesting excellent light collection ability from ultraviolet to visible light regions. Notably, the CdS QDs-30%Co<sub>9</sub>S<sub>8</sub> composite displays superior light harvesting capability compared to CdS alone, which indicates the enhanced light absorption achieved through the introduction of the Co<sub>9</sub>S<sub>8</sub> cocatalyst in the composite photocatalyst.

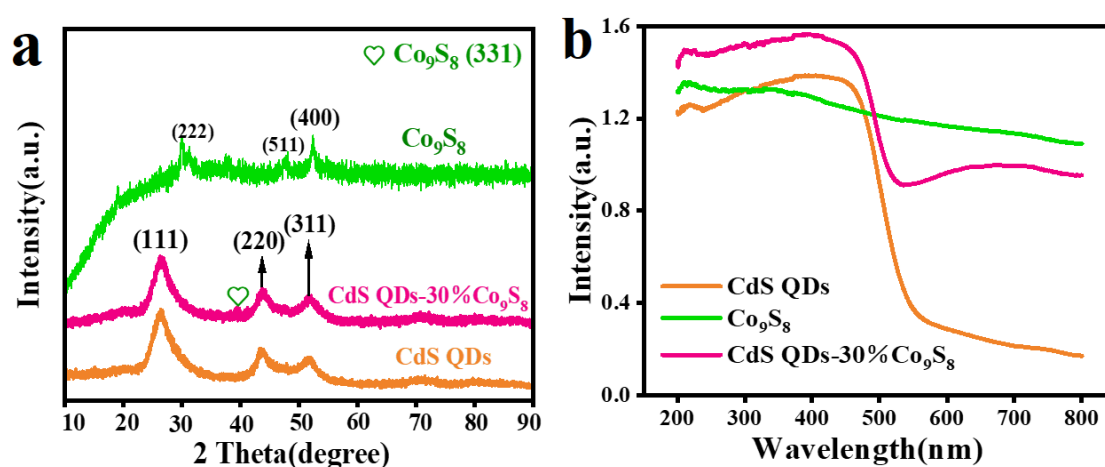


**Figure 4.** (a) XRD pattern of blank CdS QDs, Co<sub>9</sub>S<sub>8</sub> and CdS QDs-30%Co<sub>9</sub>S<sub>8</sub> composite. (b) UV-vis diffuse reflection spectra of blank CdS QDs, Co<sub>9</sub>S<sub>8</sub> and CdS QDs-30%Co<sub>9</sub>S<sub>8</sub> composite.

X-ray photoelectron spectroscopy (XPS) analysis (Figure 5) of the CdS QDs-30%Co<sub>9</sub>S<sub>8</sub> composite is performed in order to further determine the chemical state and elemental composition of the prepared sample. As the survey spectra shown in Figure 5a, Co, Cd and S elements are present in the CdS QDs-30%Co<sub>9</sub>S<sub>8</sub> composite, which further confirms the successful assembly of CdS QDs and Co<sub>9</sub>S<sub>8</sub> cocatalyst. In the XPS spectra of Cd 3d (Figure 5b), the two characteristic peaks at 410.2 eV and 403.4 eV belong to Cd 3d<sub>3/2</sub> and Cd 3d<sub>5/2</sub>, respectively, which demonstrates Cd exists in the form of +2 valence in the binary composite photocatalyst CdS QDs-30%Co<sub>9</sub>S<sub>8</sub> [21]. As illustrated in Figure 5c, the distinct peaks at the binding energies of 160.1 eV and 161.9 eV belong to S 2p<sub>3/2</sub> and S 2p<sub>1/2</sub>, respectively, confirming the existence of S<sup>2-</sup> [28]. In addition, the XPS spectra of Co 2p displayed in Figure 5d can be divided into two spin-orbital dual peaks and two satellite peaks (identified as “Sat.”). The first dual peaks at 780.3 eV and 776.6 eV and the second dual peaks at 796.8 eV and 794.5 eV can be attributed to Co 2p<sub>3/2</sub> and Co 2p<sub>1/2</sub>, respectively, demonstrating the existence of Co<sup>2+</sup> and Co<sup>3+</sup> [29]. The XPS results confirm that the prepared composite contains CdS and Co<sub>9</sub>S<sub>8</sub>, which indicates the successful preparation of this hybrid.

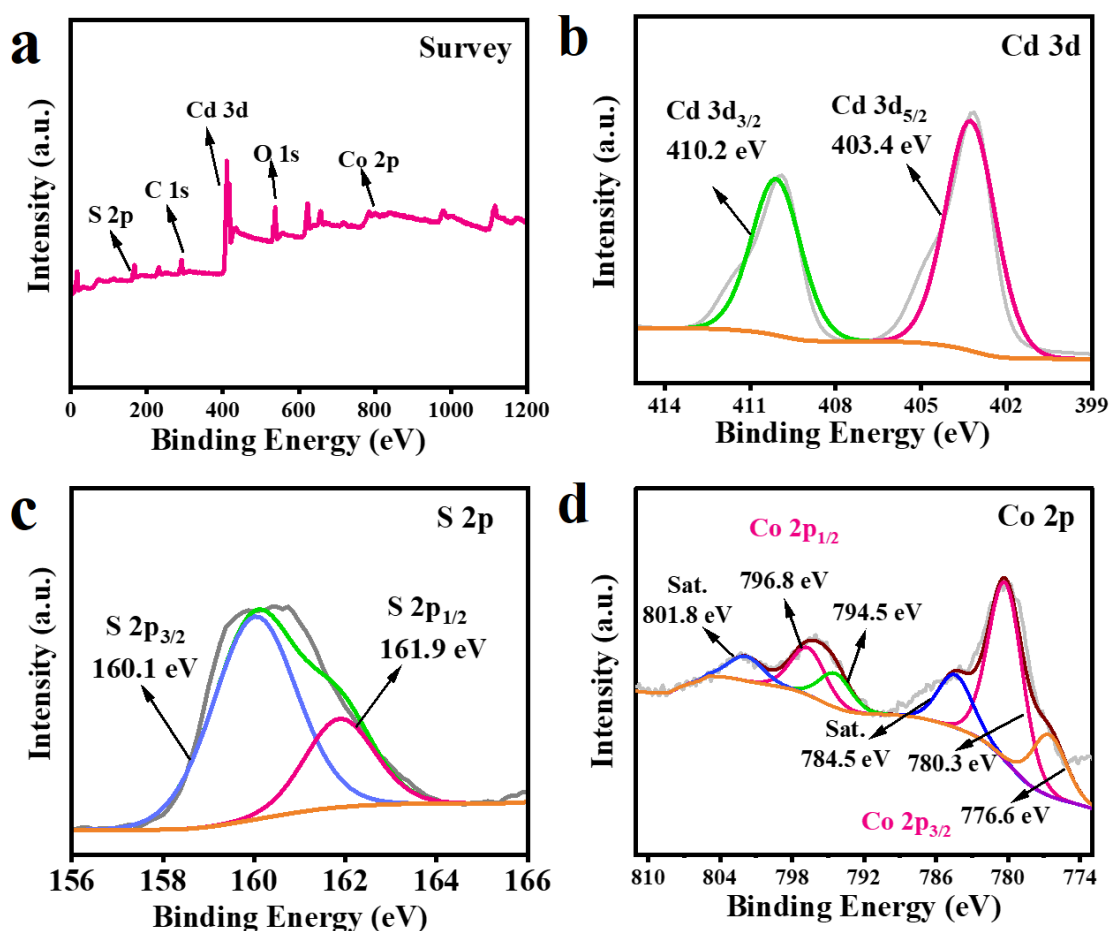


**Figure 5.** XPS spectra for (a) the survey spectra of the CdS QDs-30%Co<sub>9</sub>S<sub>8</sub> composite, (b) Cd 3d, (c) S 2p and (d) Co 2p.

In order to compare the photocatalytic performance of pure CdS QDs and CdS QDs-Co<sub>9</sub>S<sub>8</sub> composites illuminated by visible light, a photocatalytic hydrogen evolution experiment is conducted using TEOA as a sacrificial agent. As displayed in Figure 6a, on account of the serious recombination of photogenerated carriers, the blank CdS QDs exhibit low photocatalytic activity, which demonstrates a hydrogen production rate of  $159.8 \mu\text{mol}\cdot\text{g}^{-1}\cdot\text{h}^{-1}$ . When CdS QDs are combined with 5%, 10%, 30% and 50% Co<sub>9</sub>S<sub>8</sub> nanotubes, the different proportions of the CdS QDs-Co<sub>9</sub>S<sub>8</sub> composites show enhanced photocatalytic activity. As the loading capacity of Co<sub>9</sub>S<sub>8</sub> is increased, the photocatalytic H<sub>2</sub> production rate of the CdS QDs-Co<sub>9</sub>S<sub>8</sub> composites exhibits a corresponding increase. In particular, the optimal CdS QDs-30%Co<sub>9</sub>S<sub>8</sub> composite photocatalyst demonstrated a hydrogen production rate of  $9642.7 \mu\text{mol}\cdot\text{g}^{-1}\cdot\text{h}^{-1}$ , which is 60.3 times that of pure CdS QDs. Nevertheless, when the Co<sub>9</sub>S<sub>8</sub> cocatalyst content continually increased, the hydrogen production rate of the CdS QDs-Co<sub>9</sub>S<sub>8</sub> composite decreased. This phenomenon may be attributed to the high proportion of cocatalysts, which results in the masking of the CdS QDs' active sites during hydrogen evolution. As demonstrated in Table 1, the photocatalytic H<sub>2</sub> evolution rate of the CdS QDs-30%Co<sub>9</sub>S<sub>8</sub> composite is superior to that of similar photocatalysts documented in the literature. Furthermore, the photocatalytic stability of the CdS QDs-30%Co<sub>9</sub>S<sub>8</sub> composite photocatalyst is evaluated by cyclic experiment. As illustrated in Figure 6b, the CdS QDs-30%Co<sub>9</sub>S<sub>8</sub> composite photocatalyst demonstrates a stable photocatalytic activity following five cycles. These findings demonstrate that the CdS QDs-Co<sub>9</sub>S<sub>8</sub> composite is an efficacious and stable photocatalyst. In addition, Figure 6c,d demonstrate that there is no obvious change in the SEM image and XRD pattern of the CdS QDs-30%Co<sub>9</sub>S<sub>8</sub> composites following cycling, which further shows that the composites have excellent stability.

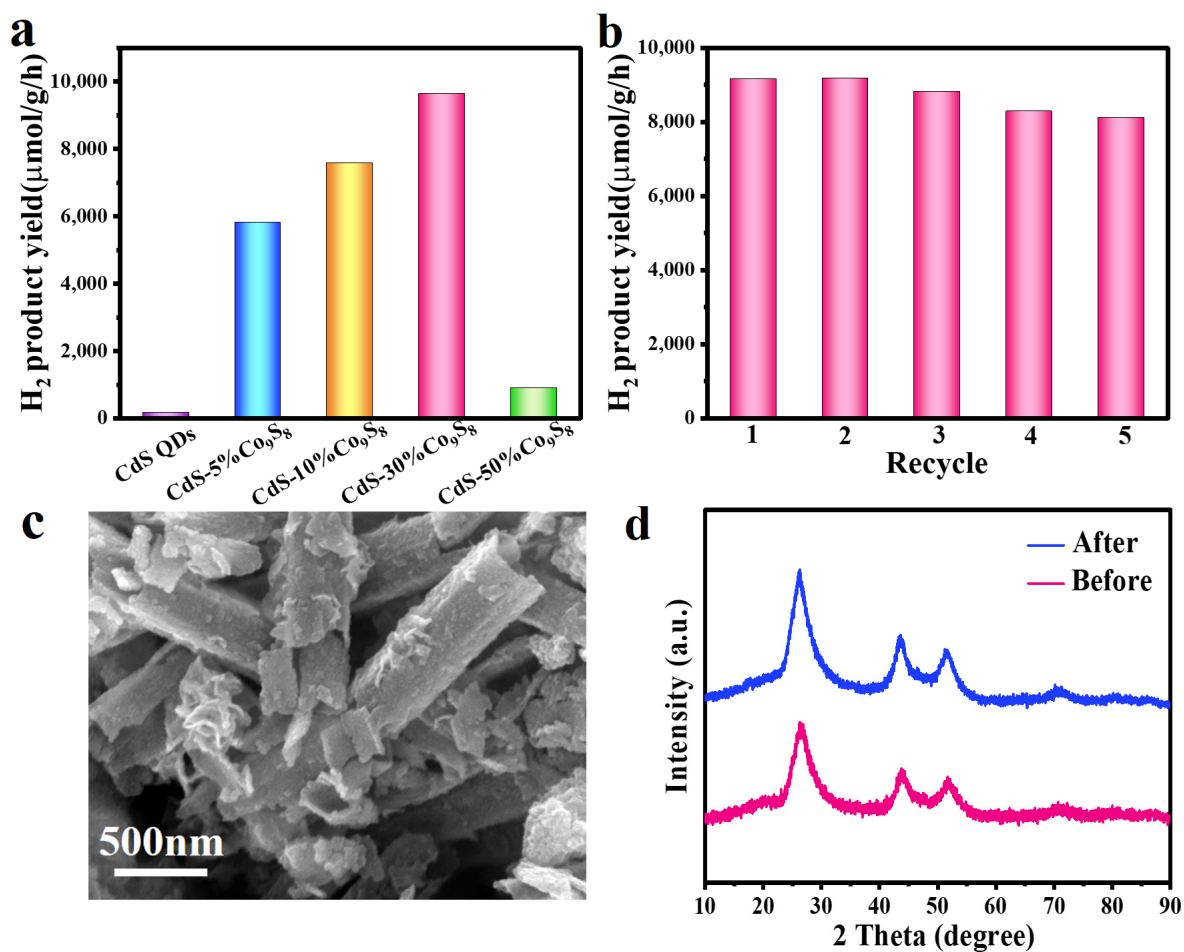


**Figure 6.** (a) Photocatalytic hydrogen production rates of blank CdS QDs and CdS QDs-Co<sub>9</sub>S<sub>8</sub> composite. (b) Cyclic stability test of CdS QDs-30%Co<sub>9</sub>S<sub>8</sub> photocatalytic hydrogen production. (c) The SEM images of CdS QDs-30%Co<sub>9</sub>S<sub>8</sub> composite after cyclic test. (d) XRD patterns of the CdS QDs-30%Co<sub>9</sub>S<sub>8</sub> before and after cyclic test.

**Table 1.** Contrast of the H<sub>2</sub> production performance of the CdS-based photocatalysts.

Photocatalysts	Light Sources	Sacrificial Agents	H <sub>2</sub> (μmol·g <sup>-1</sup> ·h <sup>-1</sup> )	Reference
CdS QDs-30% Co <sub>9</sub> S <sub>8</sub>	300 W Xe lamp (λ ≥ 420 nm)	TEOA	9642.7	this work
CdS/TiO <sub>2</sub> @Ti <sub>3</sub> C <sub>2</sub>	300 W Xe lamp (λ ≥ 420 nm)	TEOA	3115.0	[30]
CdS QDs/Ni <sub>2</sub> P/B-TiO <sub>2</sub>	300 W Xe arc lamp	Na <sub>2</sub> S/Na <sub>2</sub> SO <sub>3</sub>	3303.9	[31]
CdS/Au/KTaO <sub>3</sub>	Xe lamp (λ ≥ 420 nm)	Na <sub>2</sub> S/Na <sub>2</sub> SO <sub>3</sub>	2892.0	[32]
CdS QDs/CeO <sub>2</sub>	300 W Xe lamp (λ ≥ 300 nm)	Na <sub>2</sub> S/Na <sub>2</sub> SO <sub>3</sub>	101.1	[33]
Ni@NiO/CdS	500 W Xe lamp	TEOA	4380.0	[34]
CuS/CdS	300 W Xe lamp (λ ≥ 420 nm)	lactic acid (10 vol%)	5617.0	[35]
UiO-66-NH <sub>2</sub> @CdS	300 W Xe lamp (λ ≥ 420 nm)	Na <sub>2</sub> S/Na <sub>2</sub> SO <sub>3</sub>	2028.5	[36]
ZnO-Cu-CdS	300 W Xe lamp (λ ≥ 420 nm)	glycerol	4655.0	[37]
Ag <sub>2</sub> S-CdS	300 W Xe lamp (λ ≥ 420 nm)	lactic acids (2 vol%)	777.3	[38]

The separation efficiency of photogenerated carriers can be evaluated through the photoluminescence (PL) measurement. As displayed in Figure 7a, the CdS QDs-30%Co<sub>9</sub>S<sub>8</sub> composite photocatalyst exhibits lower PL intensity than blank CdS QDs, indicating that the introduction of the Co<sub>9</sub>S<sub>8</sub> cocatalyst has an effective inhibition effect on the photogenerated electron–hole pair recombination, which can enhance the photocatalytic hydrogen evolution performance [39–41]. Figure 7b shows the instantaneous photocurrent response of blank CdS QDs and CdS QDs-30%Co<sub>9</sub>S<sub>8</sub> [42]. As demonstrated in Figure 7b, the photocurrent response of CdS QDs-30%Co<sub>9</sub>S<sub>8</sub> composite is significantly higher than that of blank CdS QDs, which indicates the improved photogenerated carrier separation efficiency of the CdS QDs-30%Co<sub>9</sub>S<sub>8</sub> composite [43–45]. Additionally, the charge migration behavior at the catalyst–electrolyte interface is investigated through electrochemical impedance spectroscopy (EIS). Generally, a smaller radius of curvature results in lower resistance for the catalyst during the charge transfer process. As we can see from the EIS Nyquist diagram (Figure 7c), the CdS QDs-30%Co<sub>9</sub>S<sub>8</sub> composite exhibits a smaller curvature radius than that of the CdS QDs, which demonstrates that the CdS QDs-30%Co<sub>9</sub>S<sub>8</sub> composite represents a faster-photogenerated carrier transfer rate and a lower charge transfer resistance [46–49]. As displayed in Figure 7d,e, both CdS QDs and Co<sub>9</sub>S<sub>8</sub> exhibit type IV isotherms in their N<sub>2</sub> adsorption–desorption isotherms, indicating the mesoporous nature of these materials. The pore size distribution of CdS QDs, Co<sub>9</sub>S<sub>8</sub> and CdS QDs-30%Co<sub>9</sub>S<sub>8</sub> is illustrated in Figure S3 and Table S2, further confirming their mesoporous characteristics. Furthermore, the BET surface areas of CdS QDs and Co<sub>9</sub>S<sub>8</sub> are 1.50 m<sup>2</sup>/g and 8.23 m<sup>2</sup>/g, respectively, while that of CdS QDs-30%Co<sub>9</sub>S<sub>8</sub> is 116.76 m<sup>2</sup>/g (Figure 7f). The larger BET surface area of the hybrid photocatalyst compared to that of Co<sub>9</sub>S<sub>8</sub> and CdS QDs suggests that the structure of quantum dots on hollow nanotubes can expand the catalyst's surface area, thereby enhancing the photocatalytic properties of the composite catalysts. Moreover, the N<sub>2</sub> adsorption isotherm and corresponding BET-specific surface areas of all other ratios of the composites have been investigated to identify discernible trends. As depicted in Figure S4, all composites exhibit higher BET-specific surface area than blank CdS and Co<sub>9</sub>S<sub>8</sub>, and their BET-specific surface area roughly decreases with increasing Co<sub>9</sub>S<sub>8</sub> load. This phenomenon may be attributed to the high loading amount of Co<sub>9</sub>S<sub>8</sub>, resulting in nanotube stacking and consequently reducing the composite's BET-specific surface area.

The band structure information of CdS and Co<sub>9</sub>S<sub>8</sub> can be acquired through UV–vis absorption spectra (Figure 4b) and Mott–Schottky plots (Figure 8). The band gap energy ( $E_g$ ) of the synthesized samples is determined through the Tauc equation:  $(\alpha h\nu)^2 = A(h\nu - E_g)$ , where  $\alpha$ ,  $\nu$ ,  $h$  and  $A$  are the absorption coefficient, frequency of light, Planck's constant and proportionality constant, respectively. As depicted in Figure 8a,b, CdS QDs and Co<sub>9</sub>S<sub>8</sub> exhibit  $E_g$  of 2.36 eV and 1.87 eV, respectively. The Mott–Schottky (M-S) method is employed to ascertain the semiconductor type and band potential. Figure 8c,d illustrates that both CdS and Co<sub>9</sub>S<sub>8</sub> display a positive slope, indicating their n-type semiconductor nature [50]. From the M-S diagram, it is evident that the flat band potential ( $V_{fb}$ ) for CdS QDs is  $-0.47$  V, while that of Co<sub>9</sub>S<sub>8</sub> is  $-0.29$  V (vs. Ag/AgCl). Since the conduction potential ( $E_{CB}$ ) of n-type semiconductors is approximately  $-0.2$  V negative than  $V_{fb}$ , it can be calculated that the  $E_{CB}$  of CdS and Co<sub>9</sub>S<sub>8</sub> are  $-0.67$  V and  $-0.49$  V (vs. Ag/AgCl), respectively [51]. According to the conversion relationship, we determine that the  $E_{CB}$  of CdS is  $-0.47$  V, while that of Co<sub>9</sub>S<sub>8</sub> is  $-0.29$  V (vs. NHE). Based on the  $E_g$  of CdS and Co<sub>9</sub>S<sub>8</sub>, their valence band potential ( $E_{VB}$ ) can be calculated as 1.89 V and 1.58 V using the formula  $E_{VB} = E_{CB} + E_g$ .

Based on the aforementioned characterizations, a potential mechanism for visible-light-driven photocatalytic hydrogen evolution by CdS QDs-Co<sub>9</sub>S<sub>8</sub> has been put forward. The band positions and band gaps of CdS and Co<sub>9</sub>S<sub>8</sub> have been determined through Mott–Schottky analysis and UV–vis DRS transformation plots. Since Co<sub>9</sub>S<sub>8</sub> ( $-0.29$  V) exhibits a lower conduction band potential ( $E_{CB}$ ) than CdS ( $-0.47$  V), it suggests that the photogenerated electrons from CdS will be transferred to the CB of Co<sub>9</sub>S<sub>8</sub>. As exhibited in Figure 9, the irradiation of visible light results in the excited electrons in the valence band (VB) of CdS



QDs jumping to the CB, accompanied by the generation of photogenerated holes in the VB. Due to the tight interfacial contact between CdS QDs and  $\text{Co}_9\text{S}_8$ , photogenerated electrons are transferred from the CB of CdS QDs to the CB of  $\text{Co}_9\text{S}_8$  instead of being trapped by holes. Subsequently, the electrons that have accumulated on  $\text{Co}_9\text{S}_8$  combine with  $\text{H}^+$  to form  $\text{H}_2$ . Meanwhile, the remaining photogenerated holes in the VB of CdS rapidly oxidize the sacrificial agent triethanolamine, forming a complete reaction cycle. Furthermore, the nanotube structure of  $\text{Co}_9\text{S}_8$  provides a multitude of active sites for photocatalytic hydrogen production reactions, and combined with the multiple reflections of light in the hollow structure of  $\text{Co}_9\text{S}_8$ , the photocatalytic  $\text{H}_2$  evolution performance of the CdS QDs- $\text{Co}_9\text{S}_8$  composite is significantly enhanced.

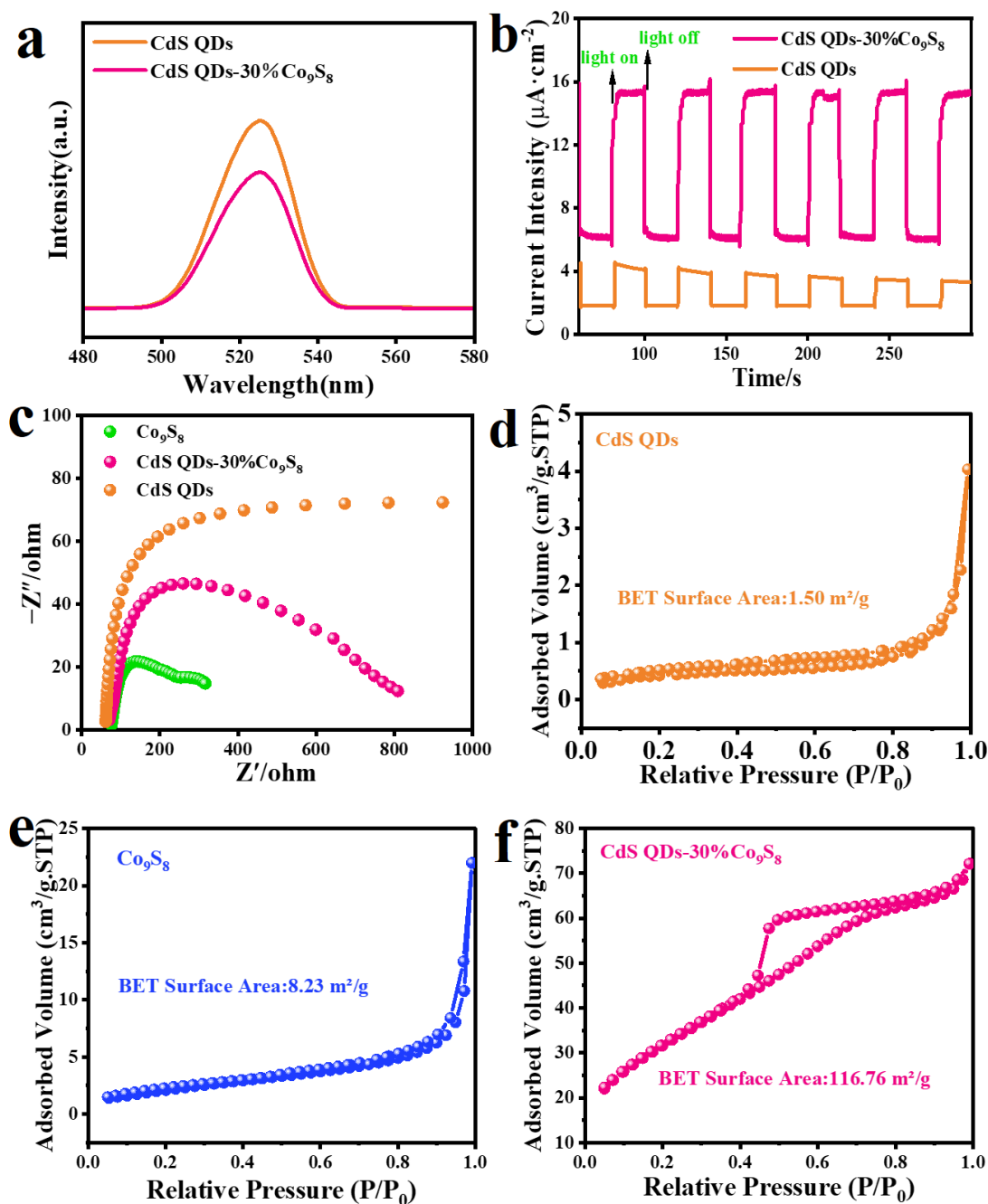


**Figure 7.** (a) Steady-state photoluminescence (PL) emission spectra with an excitation wavelength of 500 nm. (b) Transient photocurrent spectra. (c) EIS Nyquist plots. Nitrogen adsorption–desorption isotherms of (d) blank CdS QDs, (e)  $\text{Co}_9\text{S}_8$  and (f) CdS QDs-30% $\text{Co}_9\text{S}_8$  composite.

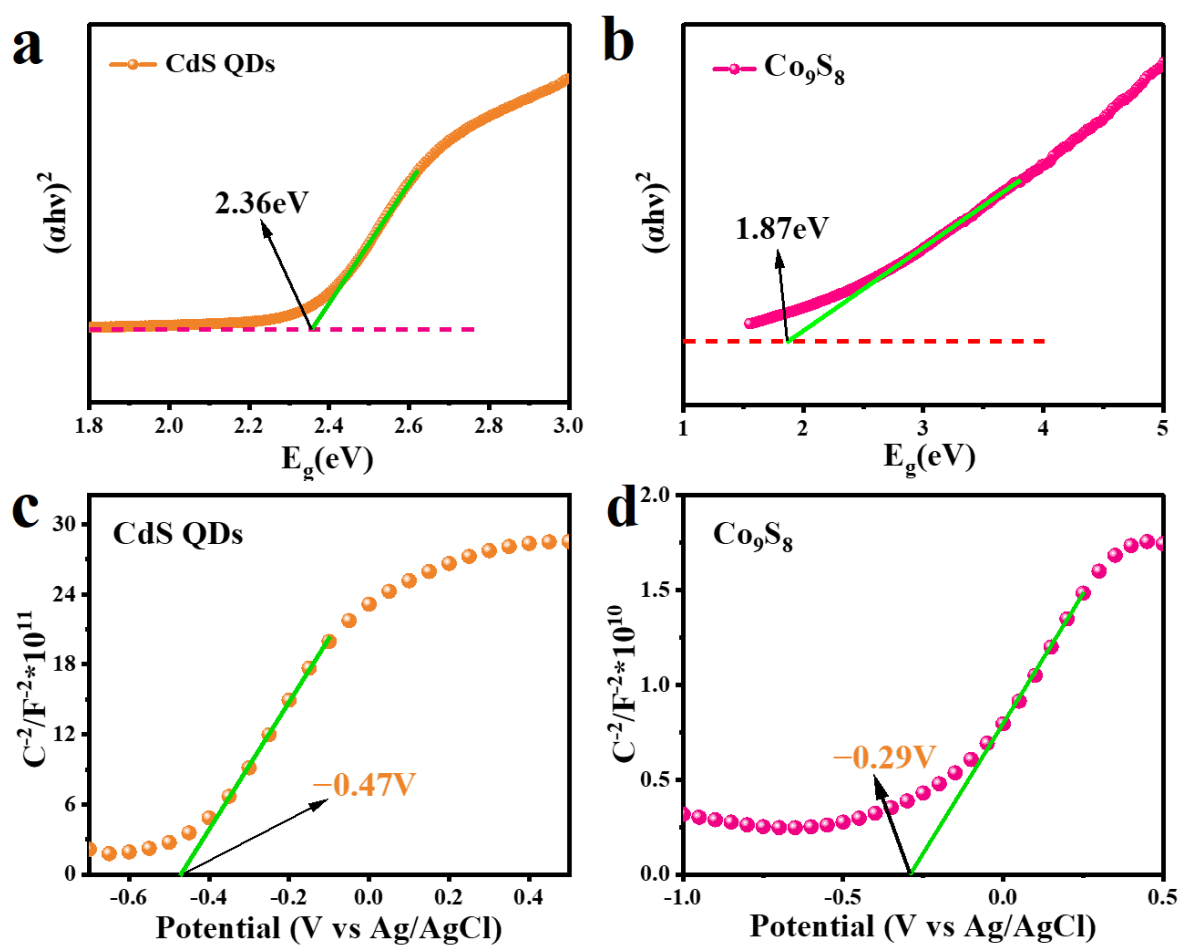


Figure 8. The band gap energy of (a) CdS QDs and (b) Co<sub>9</sub>S<sub>8</sub>. Mott-Schottky plots of (c) CdS QDs and (d) Co<sub>9</sub>S<sub>8</sub>.

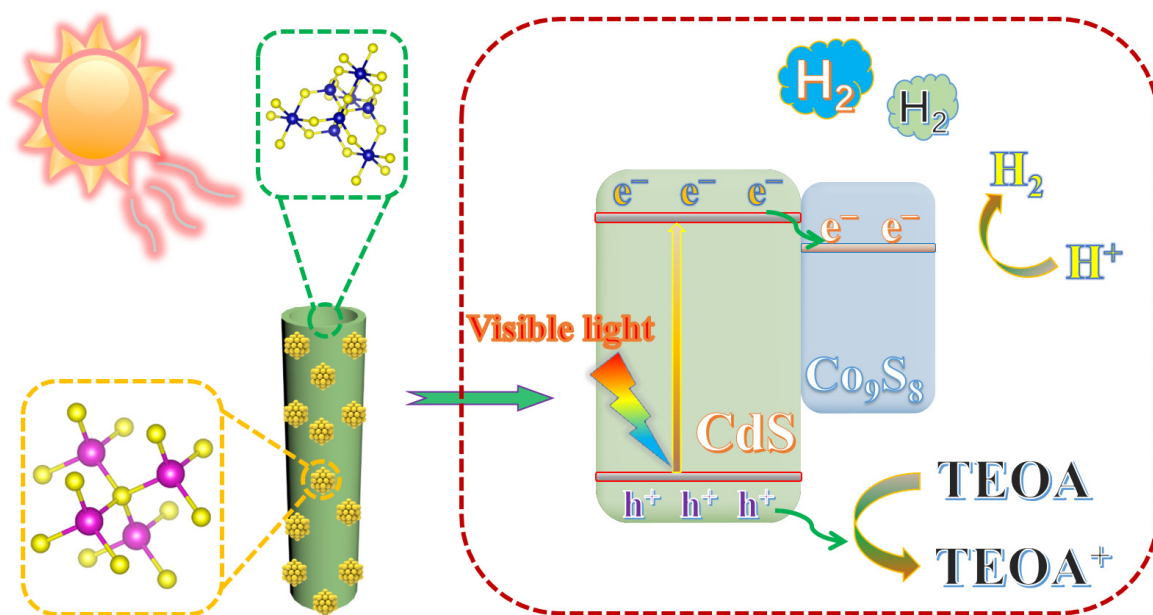


Figure 9. Mechanism diagram of CdS QDs-Co<sub>9</sub>S<sub>8</sub> in photocatalytic hydrogen production driven by visible light.

### 3. Experimental Section

#### 3.1. Materials

Anhydrous chromium chloride ( $\text{CdCl}_2$ ), sodium hydroxide ( $\text{NaOH}$ ), cobalt chloride hexahydrate ( $\text{CoCl}_2 \cdot 6\text{H}_2\text{O}$ ), 3-aminopropyl triethoxysilane (APTES) and 3-mercaptopropionic acid ( $\text{C}_3\text{H}_6\text{O}_2\text{S}$ , MPA) were supplied by Shanghai Macklin Biochemical Co., Ltd. (Shanghai, China). Triethanolamine ( $\text{C}_6\text{H}_{15}\text{NO}_3$ , TEOA) and anhydrous ethanol ( $\text{C}_2\text{H}_6\text{O}$ ) were purchased from Xilong Scientific Co., Ltd. (Shantou, China). Sodium sulfide 9-hydrate ( $\text{Na}_2\text{S} \cdot 9\text{H}_2\text{O}$ ) was supplied by Shanghai Aladdin Biochemical Technology Co., Ltd. (Shanghai, China). Urea ( $\text{CH}_4\text{N}_2\text{O}$ ) was purchased from Sinopharm Chemical Reagent Co., Ltd. (Shanghai, China).

#### 3.2. Preparation of CdS QDs

In a typical experiment, 1.7 mmol MPA (3-mercaptopropionic acid) and 1 mmol  $\text{CdCl}_2$  were dissolved in 20 mL of deionized water. The pH was then modulated to about 10 through the addition of sodium hydroxide solution. The resulting solution was then diverted into a three-necked flask, which was sealed and the air outlet preserved. Subsequently, 5 mL of  $\text{Na}_2\text{S}$  solution (0.2 mol/L) was added to the above solution in an atmosphere of argon gas and magnetically stirred. The solution was then heated to 373 K, after which the yellow solution was agitated for 0.5 h. Once the solution had cooled, 50 mL of ethanol was added to precipitate it. The resulting yellowish product was obtained after extraction, filtration, washing and drying.

#### 3.3. Preparation of $\text{Co}_9\text{S}_8$ Nanotubes

The preparation process of  $\text{Co}_9\text{S}_8$  nanotubes referred to the two-step hydrothermal method in previous work [52,53]. Firstly,  $\text{Co}(\text{CO}_3)_{0.35}\text{Cl}_{0.20}(\text{OH})_{1.10}$  nanorods were synthesized as a precursor for  $\text{Co}_9\text{S}_8$  nanotubes. This was achieved by dissolving  $\text{CoCl}_2 \cdot 6\text{H}_2\text{O}$  (5 mmol) and  $\text{CH}_4\text{N}_2\text{O}$  (5 mmol) in 40 mL deionized water and ultrasounding the solution for 30 min. Subsequently, the solution was diverted into a 50 mL Teflon autoclave and reacted in a 393 K oven for 10 h. The precipitate was then gathered through centrifugation and washed multiple times with anhydrous ethanol and deionized water. The pink precursor was obtained following drying at 333 K for several hours. Subsequently, the synthesized  $\text{Co}(\text{CO}_3)_{0.35}\text{Cl}_{0.20}(\text{OH})_{1.10}$  precursors (110 mg) were mixed to 40 mL of  $\text{Na}_2\text{S}$  solution (5 mg/mL) in the Teflon liner and stirred for an hour. The liner was then diverted into a stainless-steel autoclave and heated to a temperature of 433 K for a period of 8 h. During the vulcanization process, the inner material of the rod-like precursor underwent a reaction and fell off, thereby obtaining the  $\text{Co}_9\text{S}_8$  of the hollow nanotube structure. Subsequently, the product was isolated through suction filtration, washed with anhydrous ethanol and deionized water and dried at 333 K for 12 h, and the dried product (black powder) was collected for further processing.

#### 3.4. Positive Electrochemical Treatment of $\text{Co}_9\text{S}_8$ Nanotubes

The prepared 100 mg  $\text{Co}_9\text{S}_8$  nanotubes were dispersed in 50 mL  $\text{C}_2\text{H}_5\text{OH}$  and ultrasonic until the solution was uniform. Then, 2 mL of APTES (3-aminopropyl triethoxysilane) solution was added to the ultrasonic-treated  $\text{Co}_9\text{S}_8$  nanotube ethanol solution and stirred for 20 min. Subsequently, the product was maintained in a water bath at 333 K for a period of four hours, centrifuged and washed with anhydrous ethanol and deionized water on several occasions. The obtained product was then dried in a 333 K oven and collected for use.

#### 3.5. Electrostatic Assembly of CdS QDs- $\text{Co}_9\text{S}_8$

Typically, 50 mg CdS QDs was dispersed in 50 mL deionized water and ultrasounded for 5 min. A certain proportion of 5%/10%/30% (2.5 mg/5 mg/15 mg) electropositive  $\text{Co}_9\text{S}_8$  nanotubes were dispersed in deionized water by the same method described above and ultrasonic. After ultrasound, the  $\text{Co}_9\text{S}_8$  nanotube solution was injected into the CdS QDs solution and stirred for a period of 2.5 h. Subsequently, the mixed solution was

subjected to centrifugation and multiple washes with deionized water, after which it was dried in an oven at 333 K to yield the dried yellowish-green product.

### 3.6. Activity Evaluation of Photocatalytic H<sub>2</sub> Evolution

Photocatalytic H<sub>2</sub> production was conducted within a 50 mL closed quartz reactor. Typically, 1 mL of triethanolamine (TEOA) and 5 mL of deionized water were added to a sealed quartz reactor containing 5 mg of CdS QDs-Co<sub>9</sub>S<sub>8</sub> composite photocatalyst, followed by ultrasound until the solution was uniform. Subsequently, pure argon gas was implanted into the quartz reactor for half an hour to remove residuary air. A 300 W xenon lamp (PLS-SXE300D, Perfectlight, Beijing, China) with an ultraviolet cut-off filter ( $\lambda \geq 420$  nm) was used as the light source. Following a two-hour illumination period, 1 mL of mixed gas was injected into the gas chromatograph (GC7900, Techcomp, Shanghai, China) to detect the peak areas of hydrogen and argon, and the hydrogen production rate of the photocatalyst was then converted according to the hydrogen production coefficient given. Additionally, the stability of the CdS QDs-Co<sub>9</sub>S<sub>8</sub> composite photocatalyst was evaluated by conducting tests for 5 cycles under the same conditions after centrifugation, washing and drying.

## 4. Conclusions

In summary, Co<sub>9</sub>S<sub>8</sub> hollow nanotubes were prepared through a two-step hydrothermal approach as a cocatalyst, and the CdS QDs-Co<sub>9</sub>S<sub>8</sub> composite photocatalysts were successfully prepared through a straightforward electrostatic self-assembly method. The electrostatic self-assembly strategy ensures a tight interfacial contact between CdS QDs and Co<sub>9</sub>S<sub>8</sub> nanotubes. By adjusting the proportion of Co<sub>9</sub>S<sub>8</sub> nanotubes in the composite, the photocatalytic hydrogen evolution rate of the optimal CdS QDs-30%Co<sub>9</sub>S<sub>8</sub> nanotubes is 9642.7  $\mu\text{mol}\cdot\text{g}^{-1}\cdot\text{h}^{-1}$ , approximately 60.3 times that of blank CdS QDs. The cyclic experiment demonstrates that the introduction of Co<sub>9</sub>S<sub>8</sub> cocatalysts effectively prevents photocorrosion on the surface of CdS QDs. A series of characterization experiments illustrate that the introduction of Co<sub>9</sub>S<sub>8</sub> hollow nanotubes resulted in a more uniform and dispersed growth of CdS QDs particles, as well as the promotion of the separation and migration of photogenerated carriers. As a result, the CdS QDs-Co<sub>9</sub>S<sub>8</sub> composite exhibits excellent activity and stability in photocatalytic hydrogen production. This work provides new perspectives for the rational construction of stable, environmentally friendly and highly active composite photocatalysts to realize efficient photocatalytic H<sub>2</sub> evolution.

**Supplementary Materials:** The following supporting information can be downloaded at: <https://www.mdpi.com/article/10.3390/molecules29153530/s1>. Figure S1. Schematic representation of the samples for (a) CdS QDs, (b) Co<sub>9</sub>S<sub>8</sub> and (c) CdS QDs-Co<sub>9</sub>S<sub>8</sub>. Figure S2. (a) TEM image and (b) HRTEM image of Co<sub>9</sub>S<sub>8</sub>. Figure S3. Pore size distributions of (a) CdS QDs, (b) Co<sub>9</sub>S<sub>8</sub> and (c) CdS QDs-30%Co<sub>9</sub>S<sub>8</sub>. Figure S4. Nitrogen adsorption–desorption isotherms of (a) CdS QDs-5%Co<sub>9</sub>S<sub>8</sub>, (b) CdS QDs-10%Co<sub>9</sub>S<sub>8</sub> and (c) CdS QDs-50%Co<sub>9</sub>S<sub>8</sub>. Table S1. Summary of the ICP analysis results of the samples of CdS QDs-5%Co<sub>9</sub>S<sub>8</sub>, CdS QDs-10%Co<sub>9</sub>S<sub>8</sub>, CdS QDs-30%Co<sub>9</sub>S<sub>8</sub> and CdS QDs-50%Co<sub>9</sub>S<sub>8</sub>. Table S2. The average pore size distributions of the prepared photocatalysts.

**Author Contributions:** Conceptualization, Y.Y. and K.L.; methodology, C.L.; software, Y.W. (Yonghui Wu); validation, Y.W. (Yu Wei), Y.Y. and J.W.; formal analysis, K.Y.; investigation, J.-L.Z.; resources, K.L. and B.W.; data curation, Y.W. (Yonghui Wu); writing—original draft preparation, Y.Y.; writing—review and editing, K.L.; visualization, W.-Y.H.; supervision, K.L.; project administration, B.W.; funding acquisition, K.L. All authors have read and agreed to the published version of the manuscript.

**Funding:** This work was supported by Jiangxi Provincial Natural Science Foundation (No. 20224BAB203018, 20224ACB213010, 20232BAB213050, 20232ACB203022), the Jiangxi Province “Double Thousand Plan” (No. jxsq2023102143, jxsq2023102142, jxsq2023201086, jxsq2023102141, jxsq2019102053), the National Natural Science Foundation of China (No. 22366018, 5236005), the Program of Qingjiang Excellent Young Talents, JXUST (No. JXUSTQJB2020005) and Jiangxi Provincial Key Laboratory of Functional Crystalline Materials Chemistry (2024SSY05161).

**Institutional Review Board Statement:** Not applicable.

**Informed Consent Statement:** Not applicable.

**Data Availability Statement:** Data are contained within the article.

**Acknowledgments:** The authors would like to thank Chen Weiwei from Shiyanjia Lab ([www.shiyanjia.com](http://www.shiyanjia.com)) for the XPS analysis on January 2024 and Jiangxi Qianvi New Materials Co., Ltd. for SEM analysis and TEM analysis provided by zkec ([www.zkec.cc](http://www.zkec.cc)) on 1 May 2024.

**Conflicts of Interest:** The authors declare no conflicts of interest.

## References

1. Lu, K.-Q.; Li, Y.-H.; Zhang, F.; Qi, M.-Y.; Chen, X.; Tang, Z.-R.; Yamada, Y.M.A.; Anpo, M.; Conte, M.; Xu, Y.-J. Rationally designed transition metal hydroxide nanosheet arrays on graphene for artificial CO<sub>2</sub> reduction. *Nat. Commun.* **2020**, *11*, 5181. [[CrossRef](#)] [[PubMed](#)]
2. Su, Q.; Zuo, C.; Liu, M.; Tai, X. A review on Cu<sub>2</sub>O-Based composites in photocatalysis: Synthesis, modification, and applications. *Molecules* **2023**, *28*, 5576. [[CrossRef](#)] [[PubMed](#)]
3. Zheng, M.; Wu, P.; Li, L.; Yu, F.; Ma, J. Adsorption/desorption behavior of ciprofloxacin on aged biodegradable plastic PLA under different exposure conditions. *J. Environ. Chem. Eng.* **2023**, *11*, 109256. [[CrossRef](#)]
4. Li, X.-X.; Liu, X.-C.; Liu, C.; Zeng, J.-M.; Qi, X.-P. Co<sub>3</sub>O<sub>4</sub>/stainless steel catalyst with synergistic effect of oxygen vacancies and phosphorus doping for overall water splitting. *Tungsten* **2022**, *5*, 100–108. [[CrossRef](#)]
5. Luo, H.; Gao, H.; Zhang, X.; Yang, F.; Liu, C.; Xu, K.; Guo, D. Caterpillar-like 3D graphene nanoscrolls@CNTs hybrids decorated with Co-doped MoSe<sub>2</sub> nanosheets for electrocatalytic hydrogen evolution. *J. Mater. Sci. Technol.* **2023**, *136*, 43–53. [[CrossRef](#)]
6. Xiao, Y.; Jiang, Y.; Zhou, E.; Zhang, W.; Liu, Y.; Zhang, J.; Wu, X.; Qi, Q.; Liu, Z. In-suit fabricating an efficient electronic transport channels via S-scheme polyaniline/Cd<sub>0.5</sub>Zn<sub>0.5</sub>S heterojunction for rapid removal of tetracycline hydrochloride and hydrogen production. *J. Mater. Sci. Technol.* **2023**, *153*, 205–218. [[CrossRef](#)]
7. Wei, Y.; Hao, J.-G.; Zhang, J.-L.; Huang, W.-Y.; Ouyang, S.-b.; Yang, K.; Lu, K.-Q. Integrating Co(OH)<sub>2</sub> nanosheet arrays on graphene for efficient noble-metal-free EY-sensitized photocatalytic H<sub>2</sub> evolution. *Dalton Trans.* **2023**, *52*, 13923–13929. [[CrossRef](#)]
8. Wu, Y.; Wang, Z.; Yan, Y.; Wei, Y.; Wang, J.; Shen, Y.; Yang, K.; Weng, B.; Lu, K. Rational photodeposition of cobalt phosphate on flower-like ZnIn<sub>2</sub>S<sub>4</sub> for efficient photocatalytic hydrogen evolution. *Molecules* **2024**, *29*, 465. [[CrossRef](#)]
9. Wu, K.; Shang, Y.; Li, H.; Wu, P.; Li, S.; Ye, H.; Jian, F.; Zhu, J.; Yang, D.; Li, B.; et al. Synthesis and hydrogen production performance of MoP/a-TiO<sub>2</sub>/Co-ZnIn<sub>2</sub>S<sub>4</sub> flower-like composite photocatalysts. *Molecules* **2023**, *28*, 4350. [[CrossRef](#)]
10. Yuan, H.; Mei, J.-H.; Gong, Y.-N.; Zhong, D.-C.; Lu, T.-B. Cobalt-based heterogeneous catalysts for photocatalytic carbon dioxide reduction. *Tungsten* **2023**, *6*, 410–421. [[CrossRef](#)]
11. Yan, Y.Q.; Wu, Y.Z.; Wu, Y.H.; Weng, Z.L.; Liu, S.J.; Liu, Z.G.; Lu, K.Q.; Han, B. Recent Advances of CeO<sub>2</sub>-Based Composite Materials for Photocatalytic Applications. *ChemSusChem* **2024**, *17*, e202301778. [[CrossRef](#)]
12. Camara, F.; Gavaggio, T.; Dautreppe, B.; Chauvin, J.; Pécaut, J.; Aldakov, D.; Collomb, M.-N.; Fortage, J. Electrochemical properties of a rhodium(III) mono-terpyridyl complex and use as a catalyst for light-driven hydrogen evolution in water. *Molecules* **2022**, *27*, 6614. [[CrossRef](#)] [[PubMed](#)]
13. Xie, S.; Wang, Z.; Cheng, F.; Zhang, P.; Mai, W.; Tong, Y. Ceria and ceria-based nanostructured materials for photoenergy applications. *Nano Energy* **2017**, *34*, 313–337. [[CrossRef](#)]
14. Wang, J.-H.; Yang, S.-W.; Ma, F.-B.; Zhao, Y.-K.; Zhao, S.-N.; Xiong, Z.-Y.; Cai, D.; Shen, H.-D.; Zhu, K.; Zhang, Q.-Y.; et al. RuCo alloy nanoparticles embedded within N-doped porous two-dimensional carbon nanosheets: A high-performance hydrogen evolution reaction catalyst. *Tungsten* **2023**, *6*, 114–123. [[CrossRef](#)]
15. Gao, R.; Bai, J.; Shen, R.; Hao, L.; Huang, C.; Wang, L.; Liang, G.; Zhang, P.; Li, X. 2D/2D covalent organic framework/CdS Z-scheme heterojunction for enhanced photocatalytic H<sub>2</sub> evolution: Insights into interfacial charge transfer mechanism. *J. Mater. Sci. Technol.* **2023**, *137*, 223–231. [[CrossRef](#)]
16. Lu, K.-Q.; Chen, Y.; Xin, X.; Xu, Y.-J. Rational utilization of highly conductive, commercial Elicarb graphene to advance the graphene-semiconductor composite photocatalysis. *Appl. Catal. B Environ.* **2018**, *224*, 424–432. [[CrossRef](#)]
17. Mehdi Sabzehmeidani, M.; Karimi, H.; Ghaedi, M. CeO<sub>2</sub> nanofibers-CdS nanostructures n-n junction with enhanced visible-light photocatalytic activity. *Arab. J. Chem.* **2020**, *13*, 7583–7597. [[CrossRef](#)]
18. Yue, D.; Qian, X.; Kan, M.; Ren, M.; Zhu, Y.; Jiang, L.; Zhao, Y. Sulfurated [NiFe]-based layered double hydroxides nanoparticles as efficient co-catalysts for photocatalytic hydrogen evolution using CdTe/CdS quantum dots. *Appl. Catal. B* **2017**, *209*, 155–160. [[CrossRef](#)]
19. Zhang, Z.; Rogers, C.R.; Weiss, E.A. Energy transfer from CdS QDs to a photogenerated Pd complex enhances the rate and selectivity of a Pd-photocatalyzed heck reaction. *J. Am. Chem. Soc.* **2019**, *142*, 495–501. [[CrossRef](#)]
20. Zhang, Y.; Zhou, W.; Tang, Y.; Guo, Y.; Geng, Z.; Liu, L.; Tan, X.; Wang, H.; Yu, T.; Ye, J. Unravelling unsaturated edge S in amorphous NiS<sub>x</sub> for boosting photocatalytic H<sub>2</sub> evolution of metastable phase CdS confined inside hydrophilic beads. *Appl. Catal. B Environ.* **2022**, *305*, 121055. [[CrossRef](#)]

21. Li, Y.-H.; Qi, M.-Y.; Li, J.-Y.; Tang, Z.-R.; Xu, Y.-J. Noble metal free CdS@CuS-NixP hybrid with modulated charge transfer for enhanced photocatalytic performance. *Appl. Catal. B Environ.* **2019**, *257*, 117934. [[CrossRef](#)]
22. Ma, X.; Lei, Z.; Wang, C.; Fu, Z.; Hu, X.; Fan, J.; Liu, E. Fabrication of P-doped Co<sub>9</sub>S<sub>8</sub>/g-C<sub>3</sub>N<sub>4</sub> heterojunction for excellent photocatalytic hydrogen evolution. *Int. J. Hydrogen Energy* **2021**, *46*, 36781–36791. [[CrossRef](#)]
23. Larimi, A.; Rahimi, M.; Khorasheh, F. Carbonaceous supports decorated with Pt–TiO<sub>2</sub> nanoparticles using electrostatic self-assembly method as a highly visible-light active photocatalyst for CO<sub>2</sub> photoreduction. *Renew. Energ.* **2020**, *145*, 1862–1869. [[CrossRef](#)]
24. Chen, Z.; Wan, S.; Cheng, B.; Wang, W.; Xiang, Y.; Yu, J.; Cao, S. Efficient overall photosynthesis of H<sub>2</sub>O<sub>2</sub> by the BTz@Mn<sub>0.2</sub>Cd<sub>0.8</sub>S S-scheme heterojunction. *Sci. China Chem.* **2024**, *67*, 1953–1960. [[CrossRef](#)]
25. Kandi, D.; Martha, S.; Thirumurugan, A.; Parida, K.M. Modification of BiOI microplates with CdS QDs for enhancing stability, Optical property, Electronic behavior toward rhodamine B decolorization, and photocatalytic hydrogen evolution. *J. Phys. Chem. C* **2017**, *121*, 4834–4849. [[CrossRef](#)]
26. Feng, C.; Chen, Z.; Jing, J.; Sun, M.; Han, J.; Fang, K.; Li, W. Synergistic effect of hierarchical structure and Z-scheme heterojunction constructed by CdS nanoparticles and nanoflower-structured Co<sub>9</sub>S<sub>8</sub> with significantly enhanced photocatalytic hydrogen production performance. *J. Photochem. Photobiol. A Chem.* **2021**, *409*, 113160. [[CrossRef](#)]
27. Liu, Z.-G.; Wei, Y.; Xie, L.; Chen, H.-Q.; Wang, J.; Yang, K.; Zou, L.-X.; Deng, T.; Lu, K.-Q. Decorating CdS with cobaltous hydroxide and graphene dual cocatalyst for photocatalytic hydrogen production coupled selective benzyl alcohol oxidation. *Mol. Catal.* **2024**, *553*, 113738. [[CrossRef](#)]
28. Jiang, X.; Fan, D.; Yao, X.; Dong, Z.; Li, X.; Ma, S.; Liu, J.; Zhang, D.; Li, H.; Pu, X.; et al. Highly efficient flower-like ZnIn<sub>2</sub>S<sub>4</sub>/CoFe<sub>2</sub>O<sub>4</sub> photocatalyst with p-n type heterojunction for enhanced hydrogen evolution under visible light irradiation. *J. Colloid Interface Sci.* **2023**, *641*, 26–35. [[CrossRef](#)]
29. Ma, M.-Y.; Yu, H.-Z.; Deng, L.-M.; Wang, L.-Q.; Liu, S.-Y.; Pan, H.; Ren, J.-W.; Maximov, M.Y.; Hu, F.; Peng, S.-J. Interfacial engineering of heterostructured carbon-supported molybdenum cobalt sulfides for efficient overall water splitting. *Tungsten* **2023**, *5*, 589–597. [[CrossRef](#)]
30. Nagoor Meeran, M.; Haridharan, N.; Shkir, M.; Algarni, H.; Reddy Minnam Reddy, V. Rationally designed 1D CdS/TiO<sub>2</sub>@Ti<sub>3</sub>C<sub>2</sub> multi-components nanocomposites for enhanced visible light photocatalytic hydrogen production. *Chem. Phys. Lett.* **2022**, *809*, 140150. [[CrossRef](#)]
31. Pan, J.; Ou, W.; Li, S.; Chen, Y.; Li, H.; Liu, Y.; Wang, J.; Song, C.; Zheng, Y.; Li, C. Photocatalytic hydrogen production enhancement of Z-Scheme CdS quantum dots/Ni<sub>2</sub>P/Black Ti<sup>3+</sup>-TiO<sub>2</sub> nanotubes with dual-functional Ni<sub>2</sub>P nanosheets. *Int. J. Hydrogen Energy* **2020**, *45*, 33478–33490. [[CrossRef](#)]
32. Zhang, N.; Wu, X.; Lv, K.; Chu, Y.; Wang, G.; Zhang, D. Synthesis and highly efficient photocatalysis applications of CdS QDs and Au NPs Co-modified KTaO<sub>3</sub> perovskite cubes. *Phys. Chem. Chem. Phys.* **2023**, *25*, 14028–14037. [[CrossRef](#)] [[PubMed](#)]
33. Ma, Y.; Bian, Y.; Liu, Y.; Zhu, A.; Wu, H.; Cui, H.; Chu, D.; Pan, J. Construction of Z-Scheme system for enhanced photocatalytic H<sub>2</sub> evolution based on CdS quantum dots/CeO<sub>2</sub> nanorods heterojunction. *ACS Sustain. Chem. Eng.* **2018**, *6*, 2552–2562. [[CrossRef](#)]
34. Zhang, L.; Zhu, X.; Zhao, Y.; Zhang, P.; Chen, J.; Jiang, J.; Xie, T. The photogenerated charge characteristics in Ni@NiO/CdS hybrids for increased photocatalytic H<sub>2</sub> generation. *RSC Adv.* **2019**, *9*, 39604–39610. [[CrossRef](#)]
35. Zhang, F.; Zhuang, H.-Q.; Zhang, W.; Yin, J.; Cao, F.-H.; Pan, Y.-X. Noble-metal-free CuS/CdS photocatalyst for efficient visible-light-driven photocatalytic H<sub>2</sub> production from water. *Catal. Today* **2019**, *330*, 203–208. [[CrossRef](#)]
36. Fang, M.; Yang, Z.; Guo, Y.; Xia, X.; Pan, S. Piezoelectric effect achieves efficient carriers' spatial separation and enhanced photocatalytic H<sub>2</sub> evolution of UiO-66-NH<sub>2</sub>@CdS by transforming charge transfer mechanism. *Sep. Purif. Technol.* **2024**, *328*, 125069. [[CrossRef](#)]
37. Ahmad, I.; Shukrullah, S.; Naz, M.Y.; Bhatti, H.N. A Cu medium designed Z-scheme ZnO–Cu–CdS heterojunction photocatalyst for stable and excellent H<sub>2</sub> evolution, methylene blue degradation, and CO<sub>2</sub> reduction. *Dalton Trans.* **2023**, *52*, 6343–6359. [[CrossRef](#)]
38. Lu, C.; Du, S.; Zhao, Y.; Wang, Q.; Ren, K.; Li, C.; Dou, W. Efficient visible-light photocatalytic H<sub>2</sub> evolution with heterostructured Ag<sub>2</sub>S modified CdS nanowires. *RSC Adv.* **2021**, *11*, 28211–28222. [[CrossRef](#)]
39. Wang, F.; Yu, Z.; Shi, K.; Li, X.; Lu, K.; Huang, W.; Yu, C.; Yang, K. One-pot synthesis of N-doped NiO for enhanced photocatalytic CO<sub>2</sub> reduction with efficient charge transfer. *Molecules* **2023**, *28*, 2435. [[CrossRef](#)]
40. Tan, C.-L.; Qi, M.-Y.; Tang, Z.-R.; Xu, Y.-J. Cocatalyst decorated ZnIn<sub>2</sub>S<sub>4</sub> composites for cooperative alcohol conversion and H<sub>2</sub> evolution. *Appl. Catal. B Environ.* **2021**, *298*, 120541. [[CrossRef](#)]
41. Han, C.; Zeng, Z.; Zhang, X.; Liang, Y.; Kundu, B.K.; Yuan, L.; Tan, C.-L.; Zhang, Y.; Xu, Y.-J. All-in-One: Plasmonic Janus Heterostructures for Efficient Cooperative Photoredox Catalysis. *Angew. Chem. Int. Ed. Engl.* **2024**, e202408527. [[CrossRef](#)]
42. Chen, J.; Ren, Y.; Fu, Y.; Si, Y.; Huang, J.; Zhou, J.; Liu, M.; Duan, L.; Li, N. Integration of Co single atoms and Ni clusters on defect-rich ZrO<sub>2</sub> for strong photothermal coupling boosts photocatalytic CO<sub>2</sub> reduction. *ACS Nano* **2024**, *18*, 13035–13048. [[CrossRef](#)] [[PubMed](#)]
43. Dong, P.; Xu, X.; Luo, R.; Yuan, S.; Zhou, J.; Lei, J. Postsynthetic annulation of three-dimensional covalent organic frameworks for boosting CO<sub>2</sub> photoreduction. *J. Am. Chem. Soc.* **2023**, *145*, 15473–15481. [[CrossRef](#)] [[PubMed](#)]
44. Zhang, N.; Luo, Y.-G.; Chen, Y.-H.; Zhan, J.-Y.; Wan, H.; Liu, Z.-J. Photothermal conversion boosted photocatalytic CO<sub>2</sub> reduction over S-scheme CeO<sub>2</sub>@Cu-TCPP in situ experiments and DFT calculation. *ACS Sustain. Chem. Eng.* **2023**, *11*, 4813–4824. [[CrossRef](#)]

45. Wang, A.; Zheng, Z.; Wang, H.; Chen, Y.; Luo, C.; Liang, D.; Hu, B.; Qiu, R.; Yan, K. 3D hierarchical H<sub>2</sub>-reduced Mn-doped CeO<sub>2</sub> microflowers assembled from nanotubes as a high-performance Fenton-like photocatalyst for tetracycline antibiotics degradation. *Appl. Catal. B Environ.* **2020**, *277*, 119171. [[CrossRef](#)]
46. Zhu, C.; He, Q.; Wang, W.; Du, F.; Yang, F.; Chen, C.; Wang, C.; Wang, S.; Duan, X. S-scheme photocatalysis induced by ZnIn<sub>2</sub>S<sub>4</sub> nanoribbons-anchored hierarchical CeO<sub>2</sub> hollow spheres for boosted hydrogen evolution. *J. Colloid Interface Sci.* **2022**, *620*, 253–262. [[CrossRef](#)] [[PubMed](#)]
47. Wu, Q.; Lu, D.; Zhang, B.; Kondamareddy, K.K.; Zeng, Y.; Zhang, Y.; Wang, J.; Zhou, M.; Neena, D.; Hao, H.; et al. Interfacial optimization of CeO<sub>2</sub> nanoparticles loaded two-dimensional graphite carbon nitride toward synergistic enhancement of visible-light-driven photoelectric and photocatalytic hydrogen evolution. *Int. J. Hydrogen Energy* **2022**, *47*, 2313–2326. [[CrossRef](#)]
48. Hu, M.; Wu, C.; Feng, S.; Hua, J. A high crystalline perylene-based hydrogen-bonded organic framework for enhanced photocatalytic H<sub>2</sub>O<sub>2</sub> evolution. *Molecules* **2023**, *28*, 6850. [[CrossRef](#)]
49. Hu, H.; Zhang, X.; Zhang, K.; Ma, Y.; Wang, H.; Li, H.; Huang, H.; Sun, X.; Ma, T. Construction of a 2D/2D crystalline porous materials based S-scheme heterojunction for efficient photocatalytic H<sub>2</sub> production. *Adv. Energy Mater.* **2024**, *14*, 2303638. [[CrossRef](#)]
50. Kong, D.; Fan, H.; Yin, D.; Zhang, D.; Pu, X.; Yao, S.; Su, C. AgFeO<sub>2</sub> nanoparticle/ZnIn<sub>2</sub>S<sub>4</sub> microsphere p–n heterojunctions with hierarchical nanostructures for efficient visible-light-driven H<sub>2</sub> evolution. *ACS Sustain. Chem. Eng.* **2021**, *9*, 2673–2683. [[CrossRef](#)]
51. Li, Q.; Lu, Q.; Guo, E.; Wei, M.; Pang, Y. Hierarchical Co<sub>9</sub>S<sub>8</sub>/ZnIn<sub>2</sub>S<sub>4</sub> nanoflower enables enhanced hydrogen evolution photocatalysis. *Energy Fuels* **2022**, *36*, 4541–4548. [[CrossRef](#)]
52. Li, C.; Zhao, Y.; Liu, X.; Huo, P.; Yan, Y.; Wang, L.; Liao, G.; Liu, C. Interface engineering of Co<sub>9</sub>S<sub>8</sub>/CdIn<sub>2</sub>S<sub>4</sub> ohmic junction for efficient photocatalytic H<sub>2</sub> evolution under visible light. *J. Colloid Interface Sci.* **2021**, *600*, 794–803. [[CrossRef](#)] [[PubMed](#)]
53. Zhang, G.; Chen, D.; Li, N.; Xu, Q.; Li, H.; He, J.; Lu, J. Construction of Hierarchical Hollow Co<sub>9</sub>S<sub>8</sub>/ZnIn<sub>2</sub>S<sub>4</sub> Tubular Heterostructures for Highly Efficient Solar Energy Conversion and Environmental Remediation. *Angew. Chem. Int. Ed. Engl.* **2020**, *59*, 8255–8261. [[CrossRef](#)] [[PubMed](#)]

**Disclaimer/Publisher's Note:** The statements, opinions and data contained in all publications are solely those of the individual author(s) and contributor(s) and not of MDPI and/or the editor(s). MDPI and/or the editor(s) disclaim responsibility for any injury to people or property resulting from any ideas, methods, instructions or products referred to in the content.